JOURNAL OF MATHEMATICAL ANALYSIS AND APPLICATIONS **167**, 182–202 (1992)

Bending Stress in Gear Teeth for Variable Surface Pressure Distribution

MING-HSIUNG CHEN

Department of Agricultural Machinery Engineering, National Ping-Tung Institute of Agriculture, Taiwan, Republic of China

AND

WEN-JYI WU

Department of Mechanical Engineering, Chinese Military Academy, Feng-Shang, Taiwan, Republic of China

Submitted by Dr. E. Stanley Lee

Received June 22, 1990

The bending stress in the root fillets of gear teeth having convex, circular-arc profiles has been calculated using a new analytic model for variable surface pressure distribution. The gear tooth is modeled as a wedge with the load applied at the apex. Graphs of the nondimensional bending stress variation along the tooth length are presented for 14.5°, 22.5°, and 30° normal pressure angle; 5°, 25°, and 45° helix angle, and 16, 32, and 80 normal diametral pitch. Tables of the nondimensional maximum root-fillet stress variation are presented for the variation of normal pressure angle, helix angle, and normal diametral pitch. It is shown that gears with larger helix angles or normal diametral pitches or lower normal pressure angles have higher bending stresses for the same value of allowalble surface stress. © 1992 Academic Press, Inc.

INTRODUCTION

The earliest attempt to analyze the stresses at the root of a gear tooth was the method originated by W. Lewis [1] in 1892 for spur gears. Lewis considered the gear tooth to be a cantilever beam and assumed that the critical section was located at the point where the tooth root fillet is tangent to an inscribed parabola representing a beam of uniform strength.

In the German Standard DIN 3990 [2], a nominal bending stress is used as a basis for computing the tooth strength; the dependence of the dedendum strength on the size of the fillet radius is represented by a notch-effect factor that is dependent on the material and the surface finish.

0022-247X/92 $5.00

It was later realized that the abrupt changes in tooth contour that occur in the root fillet area cause stress concentration effects, which increase the actual stress above that predicted by the Lewis equation. To count for the stress concentration, Dolan and Broghamer [3] used photoelastic models of gear teeth in order to determine the stress correction factor to be used with the Lewis formula.

The classical approach to the problem of stress determination in gear teeth rests on the cantilever beam theory, with the addition of semi-empirical "stress concentration factors" taking account of the radii of curvature in the tooth fillet [4–9].

The development of finite element techniques [10–12] now permits an exact computation of stresses. The stresses measured by Winter and Hirt [13] were compared with the stresses that had been determined photoelastically and analytically according to the method of the finite elements and the integral equation method.

Recently, however, predictions of current stress formulas were found to be inaccurate when applied to high-strength tooth forms [14]. Basically, the discrepancy arises when the gear tooth is short in height but wide in depth or thickness. This geometry violates Saint Vanant's principle, which states that elementary beam theory applies only to sections of a beam that are at large distances from both the load and the support in comparison to the depth of the beam.

Mention should be made of conformal mapping as used by Aida and Terauchi [15]. In contrast, Albert and Obenaus [16] and Errichello [17] determine by computation the stresses occurring in an equivalent wedge profile.

In this work, the bending stress in a high-strength toothform employing circular-arc profiles is analyzed using a model suggested by Shotter [14]. These gears are of "pitch-point" contact type; i.e., the maximum tooth load is concentrated near the pitch point or the middle of the tooth height. Thus, if the Lewis model were to be applied to this type of profile, it would result in a short thick beam, and it would be expected to give an inaccurate prediction of the bending stresses.

Geometry of Gear Tooth

Figure 1 shows the coordinate system and the important reference planes. The x-axis lies along the intersection of the surface of action and the tangent plane. The x'-axis lies along the intersection of the pitch plane and the tangent plane. The origin of both coordinate frames is located at the intersection of the pitch element and the tangent plane, which is also

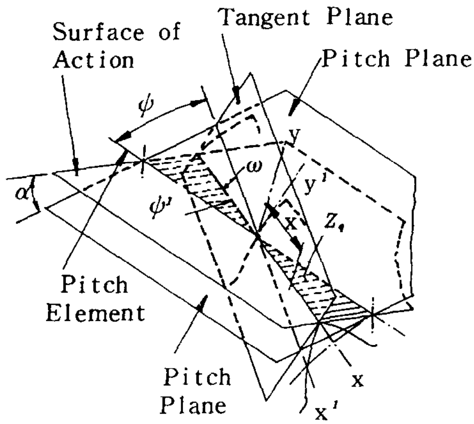

FIG. 1. Coordinate system.

the pitch point P. The y-axis and the y'-axis lie in the tangent plane. From Fig. 1

$$Z_q = x \sin \psi', \tag{1}$$

where Z_q is the distance along the line of action to a general contact point.

The pitch radii are

$$R_1 = \frac{n_1}{2\ P_n \cos \psi}; \qquad R_2 = \frac{n_2}{2P_n \cos \psi}. \tag{2}$$

The profile radii are less than the radius of curvature at the pitch point P, of corresponding involute profiles, i.e.,

$$r_1 = K_1 R_1 \sin \phi; \qquad r_2 = K_2 R_2 \sin \phi, \tag{3}$$

where $K_1 < 1$, $K_2 < 1$.

Figure shows a section taken along the line of action and the maximum boundaries of the zone of action. From Fig. 2

$$a = \frac{Z_r}{\sin \psi'}, \tag{4}$$

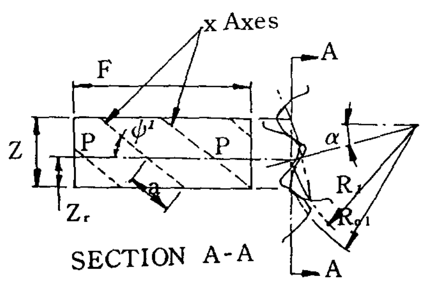

FIG. 2. Zone of action.

where Z_r is the length of the recess portion of the line of action expressed by

$$Z_r = \sqrt{R_{01}^2 - R_1^2 \cos^2 \alpha} - R_1 \sin \alpha, \tag{5}$$

where

$$T_{01} = R_1 + h \tag{6}$$

$$\tan \psi' = \frac{\tan \psi \cos \psi}{\cos(\phi - \alpha)} \tag{7}$$

$$\tan \alpha = \frac{K \sin \phi \cos \phi}{1 - K \sin^2 \phi} \tag{8}$$

$$\tan \phi_n = \tan \phi \cos \psi \tag{9}$$

$$\tan \alpha_n = \tan \alpha \cos \psi. \tag{10}$$

The geometry of the circular-arc profile is shown in Fig. 3.

$$\rho_1 = R_1 \sqrt{1 - K_1(2 - K_1) \sin^2 \phi} \tag{11}$$

$$\sin \alpha_1 = \frac{K_1 \sin \phi \cos \phi}{\sqrt{1 - K_1(2 - K_1) \sin^2 \phi}} \tag{12}$$

$$\tan \alpha_1 = \frac{K_1 \sin \phi \cos \phi}{1 - K_1 \sin^2 \phi}, \tag{13}$$

where

$$K = \frac{K_1 K_2 (1 + G)}{K_1 + G K_2}; \qquad G = n_2/n_1. \tag{14}$$

It is customary to let

$$h = 1/P_n \qquad \text{and} \qquad \gamma_1 = \pi/2n_1. \tag{15}$$

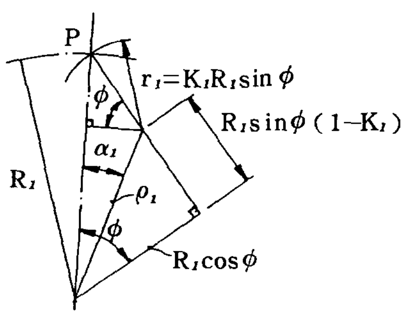

FIG. 3. Geometry of circular-arc profile.

The normal radii of profile curvature at the pitch point are

$$r_{n_1} = \frac{r_1(1 - \sin^2\psi \sin^2\phi)^{3/2}}{\cos\psi} \tag{16}$$

$$r_{n_2} = \frac{r_2}{r_1} r_{n_1}. \tag{17}$$

The relative radius or normal profile curvature is

$$\frac{1}{r_n} = \frac{1}{r_{n_1}} + \frac{1}{r_{n_2}} \tag{18}$$

i.e.,

$$r_n = \frac{r_{n_1} r_{n_2}}{r_{n_1} + r_{n_2}} = \frac{r_{n_1}(r_2/r_1)}{1 + (r_2/r_1)} = \frac{r_{n_2}(K_2 R_2/K_1 R_1)}{1 + (K_2 R_2/K_1 R_1)}$$

$$= \frac{r_{n_1}(K_2 n_2/K_1 n_1)}{1 + (K_2 n_2/K_1 n_1)} = \frac{K_2 G r_{n_1}}{K_1 + K_2 G}. \tag{19}$$

Figure 4 is a view of the hob tooth in the normal plane. The distance h_k is chosen to be slightly larger than the addendum height to avoid interference between the gear tooth fillet and the tip of the mating gear tooth. Let

$$h_k = h + \frac{0.05}{P_n} \tag{20}$$

from Fig. 4

$$\sin\phi_r = \frac{r_{nh}\sin\phi_n - h_k}{r_{nh}} \tag{21}$$

$$r_{ct} = \frac{r_{nh}\cos\phi_n + \pi/4P_n}{\cos\phi_r} - r_{nh} \tag{22}$$

$$h_b = h_k + r_{ct}(1 - \sin\phi_r), \tag{23}$$

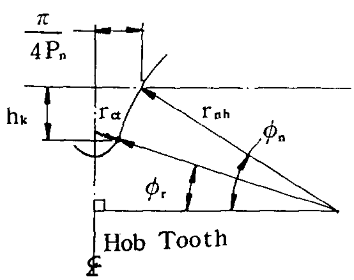

FIG. 4. Normal profile of hob.

where r_{nh} is the normal radius of the hob profile, and

$$r_{nh} = \frac{r_{nl}}{1 - K_l}. \tag{24}$$

The generated gear tooth fillet radius is nearly circular and may be approximated [18] by

$$r_{nf} = \frac{(h_b - r_{ct})^2}{R_e + (h_b - r_{ct})} + r_{ct}, \tag{25}$$

where R_e is the apparent or equivalent radius of curvature of the generating pitch circle of a helical gear tooth when viewed in the normal plane, and

$$R_e = \frac{R_1}{\cos^2 \psi}. \tag{26}$$

Bending Stress Model

Figure 5 shows the model used for this analysis. The gear tooth is considered to be a wedge loaded at its apex. The tensile stress at tangent point B and the compressive stress at tangent point C are expressed [19], respectively,

$$\sigma_t = \frac{2w_x(\sin\eta\cos\eta_c - \eta\cos\eta_t)}{l_t(\eta^2 - \sin^2\eta)} \tag{27}$$

$$\sigma_c = \frac{2w_x(\sin\eta\cos\eta_t - \eta\cos\eta_c)}{l_c(\eta^2 - \sin^2\eta)} \tag{28}$$

where

$$\eta = \eta_t - \eta_c \qquad \text{(Radians)}. \tag{29}$$

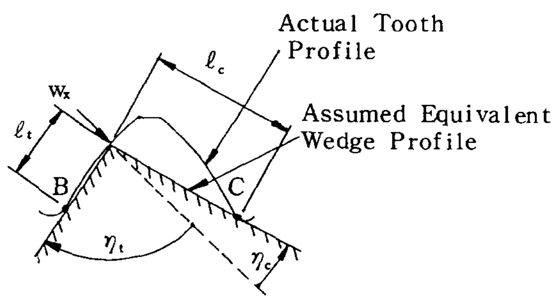

Fig. 5. Gear tooth with an inscribed wedge loaded at the apex.

These stress equations pertain to the two-dimensional case; i.e., the line load w_x is assumed to be uniformly distributed along the tip of the wedge in the thickness direction. For the circular-arc gearing considered here, both the magnitude and the position of the load on the profile change with position along the tooth length.

The theoretical contact pattern is a point where the gear teeth are unloaded, but under load the elastic deformation of the mating tooth surfaces causes the contact area to expand into a long narrow ellipse. Since the relative radius of lengthwise curvature r_l is much larger than the relative radius of normal profile curvature r_n, the contact ellipse is long and narrow. Seely and Smith [20] show that for $r_l/r_n > 50$, the area of contact is nearly a long narrow rectangle. Thus, we can assume the area of contact is a rectangle as shown in Fig. 6.

An increment of the load is equal to an increment of the volume as shown in Fig. 6, i.e.,

$$dW = 2bq\,dx, \tag{30}$$

from which the load per unit length may be found

$$w_x = \frac{dW}{dx} = 2bq, \tag{31}$$

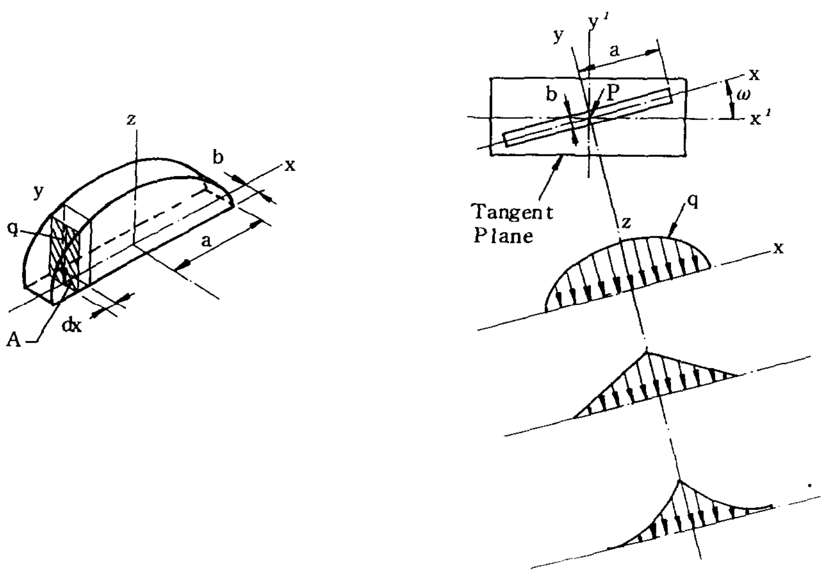

FIG. 6. Contact pattern and surface pressure distribution.

where q is the Hertzian contact stress and

$$q = q_0\left[1-\left(\frac{x}{a}\right)^n\right]. \tag{32}$$

(i) Triangular surface pressure distribution:

$$q = q_0\left[1-\left(\frac{x}{a}\right)\right], \qquad n=1. \tag{33}$$

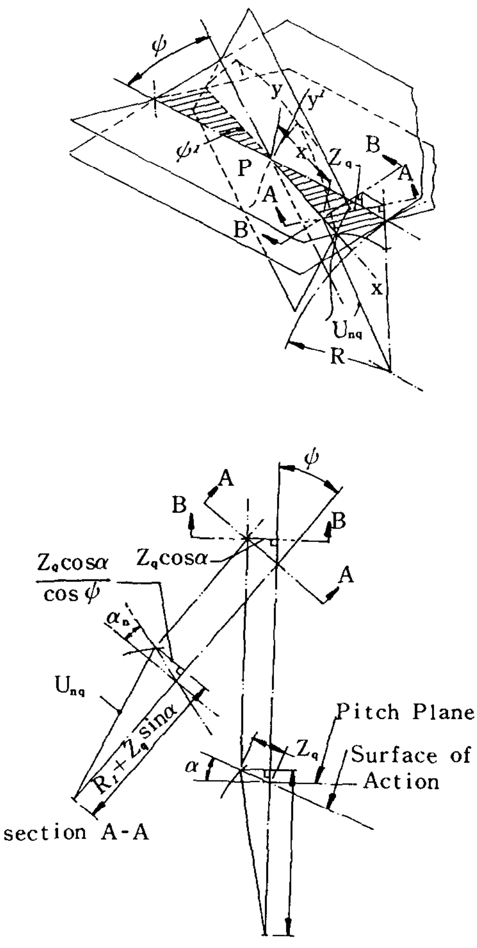

FIG. 7. Typical contact point.

(ii) Convex parabolic surface pressure distribution:

$$q = q_0\left[1 - \left(\frac{x}{a}\right)^2\right], \qquad n = 2. \tag{34}$$

(iii) Concave parabolic surface pressure distribution:

$$q = q_0\left[1 - \left(\frac{x}{a}\right)^{1/2}\right], \qquad n = \frac{1}{2}. \tag{35}$$

The half-width b of a rectangular area [19] is

$$b = 2q_0 r_n\left[\frac{1 - v_1^2}{E_1} + \frac{1 - v_2^2}{E_2}\right]. \tag{36}$$

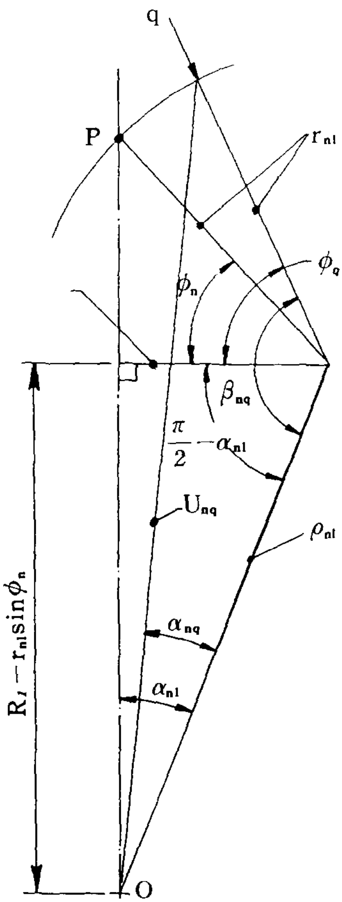

FIG. 8. Profile geometry.

Substituting Eqs. (32) and (36) into Eq. (31), we obtain

$$w_x = 4q_0^2 r_n \left[\frac{1-\nu_2^1}{E_1} + \frac{1-\nu_2^2}{E_2}\right]\left[1 - \left(\frac{x}{a}\right)^n\right]. \tag{37}$$

From Fig. 7

$$u_{n_q} = \left[\left(\frac{\cos^2\alpha}{\cos^2\psi} + \sin^2\alpha\right) Z_q^2 + 2Z_q R_1 \sin\alpha + R_1^2\right]^{1/2}. \tag{38}$$

From Fig. 8

$$\rho_{n_1} = (R_1^2 - 2R_1 r_{n_1} \sin\phi_n + r_{n_1}^2)^{1/2} \tag{39}$$

$$\sin\alpha_{n_1} = \frac{r_{n_1}\cos\phi_n}{\rho_{n_1}} \tag{40}$$

$$\cos\beta_{n_q} = \frac{r_{n_1}^2 + \rho_{n_1}^2 - u_{u_q}^2}{2r_{n_1}\rho_{n_1}} \tag{41}$$

$$\cos\alpha_{n_q} = \frac{u_{n_q}^2 + \rho_{n_1}^2 - r_{n_1}^2}{2u_{n_q}\rho_{n_1}} \tag{42}$$

$$\phi_q = \beta_{n_q} + \alpha_{n_1} - \frac{\pi}{2}. \tag{43}$$

From Figs. 9 and 10

$$l_f = R_{nr} + r_{nf} \tag{44}$$

$$R_{nr} = (R_1 - h_b)\sin\gamma_1\cos\psi/\sin\gamma_{n_1} \tag{45}$$

$$\gamma_{n_1} = \gamma_1\cos\psi. \tag{46}$$

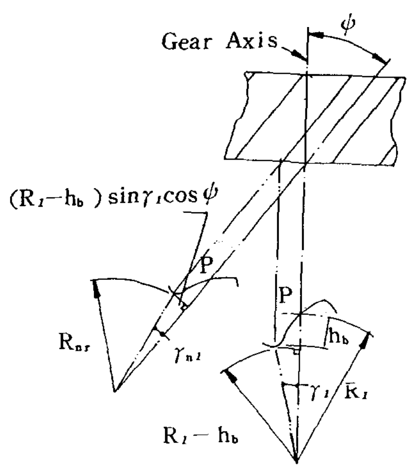

FIG. 9. Root radius in the normal plane.

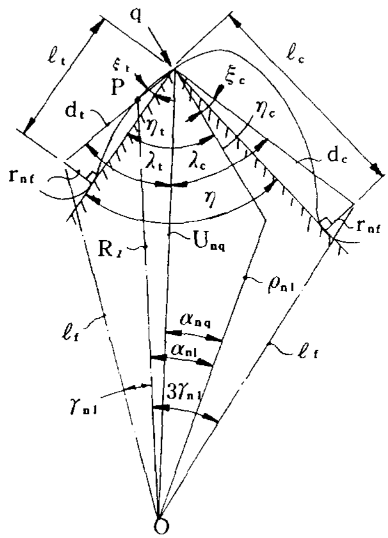

FIG. 10. Geometry of inscribed wedge model.

From Fig. 10

$$d_t = [l_f^2 + u_{n_q}^2 - 2l_f u_{n_q} \cos(\gamma_{n_l} - \alpha_{n_l} + \alpha_{n_q})]^{1/2} \tag{47}$$

$$d_c = [l_f^2 + u_{n_q}^2 - 2l_f u_{n_q} \cos(3\gamma_{n_l} - \alpha_{n_l} + \alpha_{n_q})]^{1/2} \tag{48}$$

$$l_t = (d_t^2 - r_{nf}^2)^{1/2}, \qquad l_c = (d_c^2 - r_{nf}^2)^{1/2} \tag{49}$$

$$\cos\lambda_t = \frac{d_t^2 + u_{n_q}^2 - l_f^2}{2d_t u_{n_q}}, \qquad \cos\lambda_c = \frac{d_c^2 + u_{n_q}^2 - l_f^2}{2d_c u_{n_q}} \tag{50}$$

$$\cos\xi_t = \frac{l_t}{d_t}, \qquad \cos\xi_c = \frac{l_c}{d_c} \tag{51}$$

$$\eta_t = \frac{\pi}{2} + \alpha_{n_l} - \alpha_{n_q} - \phi_q + \lambda_t - \xi_t \tag{52}$$

$$\eta_c = \frac{\pi}{2} + \alpha_{n_l} - \alpha_{n_q} - \phi_q - \lambda_c + \xi_c. \tag{53}$$

RESULTS OF COMPUTER ANALYSIS

The geometry of the wedge model shown in Fig. 10 is now fully defined. The stresses on the tension and compression side of the gear tooth may be found at any position along the tooth length. The stresses are calculated at

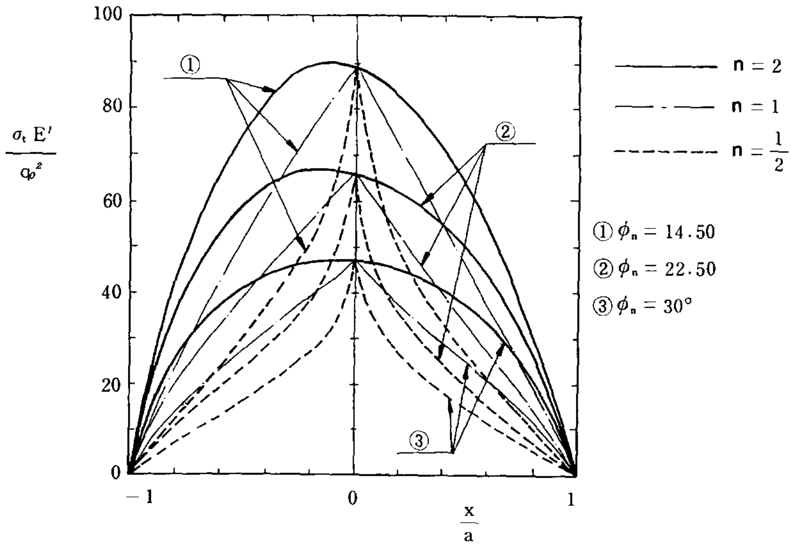

FIG. 11. Nondimensional tensile stress for $P_n = 32$ and $\psi = 45°$.

intervals along the x-axis. The contact rectangle is assumed to be tangent to the tip of the pinion tooth and to be symmetrical about the y-axis as shown in Figs. 1 and 6. At each position x, the magnitude of the load and the geometry of the wedge vary which causes the stresses also to vary with position along the tooth length.

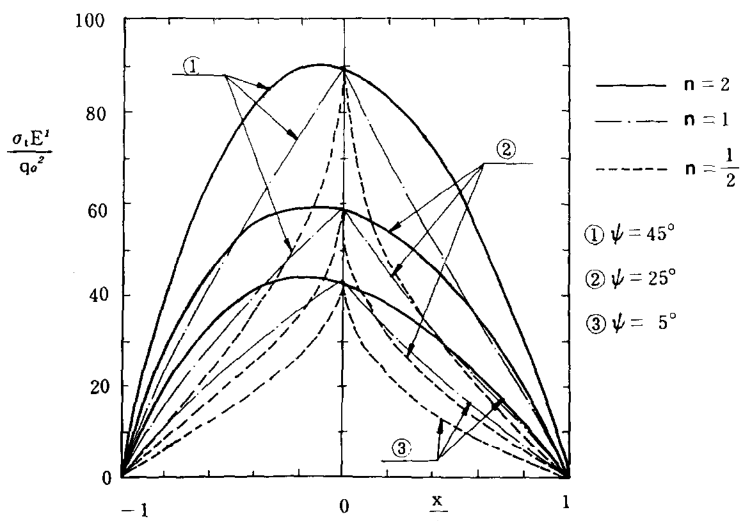

FIG. 12. Nondimensional tensile stress for $P_n = 32$ and $\phi_n = 14.5°$.

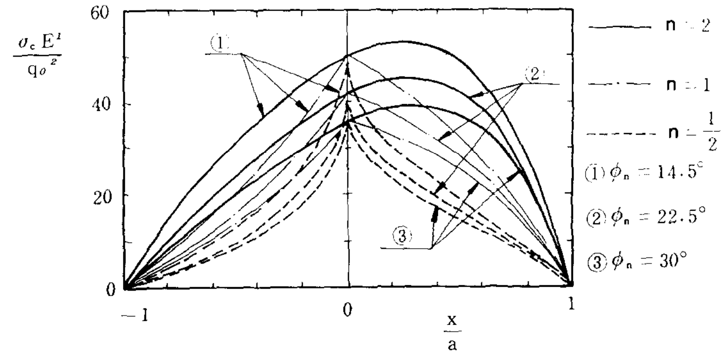

FIG. 13. Nondimensional compressive stress for $P_n = 32$ and $\psi = 45°$.

A total of 27 computer runs were made to calculate the bending stress geometries for various gear tooth for each value of n, i.e., $n = 1, 2$, and $\frac{1}{2}$. Three values of normal pressure angle, helix angle, and normal diametral pitch, respectively, were chosen as being representative of a range of practical, values as shown here:

Normal pressure angle $\phi_n = 14.5, 22.5, 30°$.

Helix angle $\psi = 5, 25, 45°$.

Normal diametral pitch $P_n = 16, 32, 80$.

The pitch radius of the pinion was arbitrarily chosen to be equal to 1 in. and the gear ratio was made equal to 2:1 in each case. The profile radius coefficients, K_1 and K_2, were selected arbitrarily for the purposes of this analysis. The allowable surface stress, q_0, is based upon the weaker of the two gear materials.

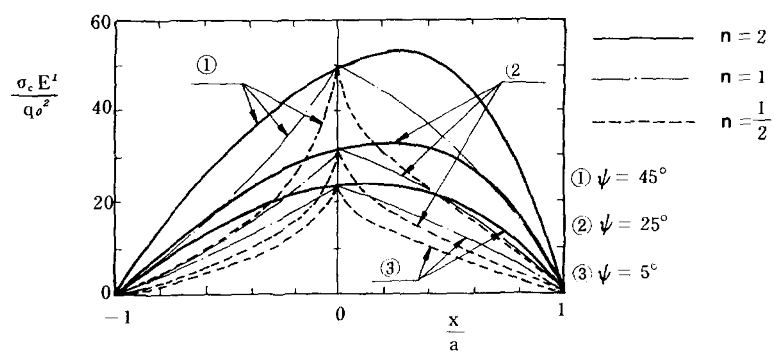

FIG. 14. Nondimensional compressive stress for $P_n = 32$ and $\phi_n = 14.5°$.

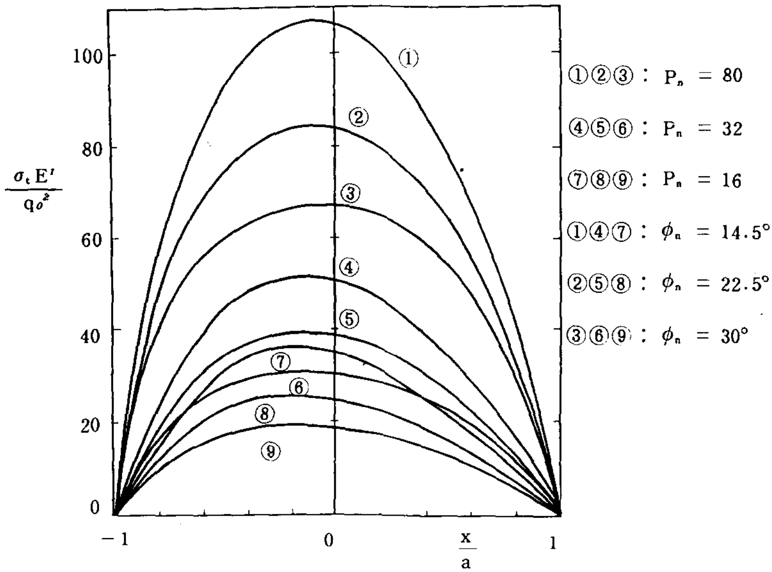

FIG. 15. Nondimensional tensile stress for $\psi = 5°$.

As shown, the stress equations are nondimensionalized in order to make the graphical results applicable to any combination of material and allowable surface stress. To make the analysis, the computed stresses were nondimensionalized as follows.

Define an effective modulus

$$\frac{1}{E'} = \frac{1 - \nu_1^2}{E_1} + \frac{1 - \nu_2^2}{E_2}. \tag{54}$$

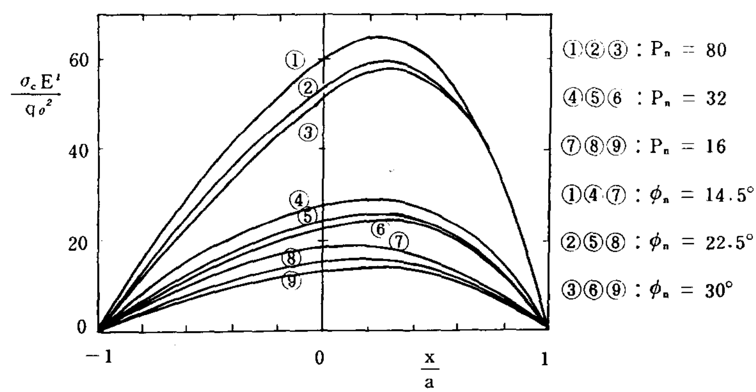

FIG. 16. Nondimensional compressive stress for $\psi = 5°$.

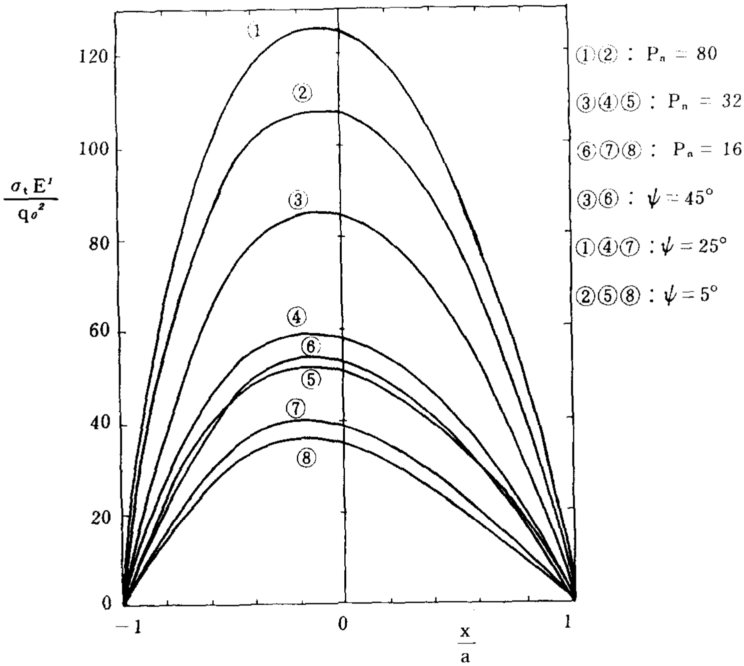

FIG. 17. Nondimensional tensile stress for $\phi_n = 14.5°$.

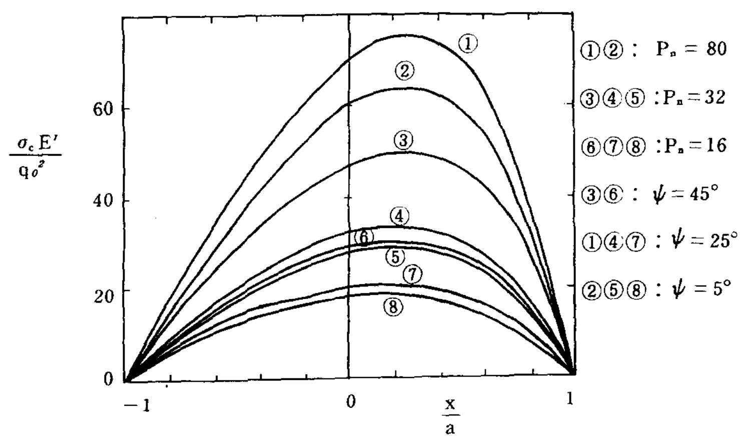

FIG. 18. Nondimensional compressive stress for $\phi_a = 14.5°$.

TABLE I

Maximum Tensile and Compressive Streses in the Fillet at the Root of the Tooth Affected by the Value of ψ and ϕ_n for $P_n = 32$

ψ	5°			25°			45°		
ϕ_n	14.5°	22.5°	30°	14.5°	22.5°	30°	14.5°	22.5°	30°
σ_{tmax}	51.8	39.5	31.0	59.3	44.0	33.4	85.6	57.4	38.9
σ_{cmax}	29.3	26.3	25.2	33.9	29.7	27.4	50.5	39.9	32.5

Substituting this value of E' into Eq. (37) gives

$$w_x = \frac{4q_0^2 r_n}{E'}\left[1 - \left(\frac{x}{a}\right)^n\right]. \tag{55}$$

Substituting Eq. (55) into Eqs. (27) and (28) gives the nondimensional stresses

$$\frac{\sigma_t E'}{q_0^2} = \frac{8r_n}{l_t}\frac{(\sin\eta\cos\eta_c - \eta\cos\eta_t)}{(\eta^2 - \sin^2\eta)}\left[1 - \left(\frac{x}{a}\right)^n\right]$$

$$\frac{\sigma_c E'}{q_0^2} = \frac{8r_n}{l_c}\frac{(\sin\eta\cos\eta_t - \eta\cos\eta_c)}{(\eta^2 - \sin^2\eta)}\left[1 - \left(\frac{x}{a}\right)^n\right],$$

where η, η_t, η_c, l_t, and l_c vary with position x.

Figs. 11–18 show graphs of typical results for the theoretical stress distribution as a function of position x. The maximum tensile and compressive stresses in the fillet at the root of the tooth affected by the variation of ψ, ϕ_n, and P_n, respectively, are presented in Tables I–III.

Discussion of Results

(1) The distribution of stress σ_t and σ_c into the fillet at the root of the tooth is similar to the form of the contact surface pressure q.

TABLE II

Maximum Tensile and Compressive Stresses in ghe Fillet at the Root of the Tooth Affected by the Value of P_n and ϕ_n for $\psi = 5°$

P_n	80			32			16		
ϕ_n	14.5°	22.5°	30°	14.5°	22.5°	30°	14.5°	22.5°	30°
σ_{tmax}	107.8	84.6	68.2	51.8	39.5	31.0	36.7	26.2	19.5
σ_{max}	64.5	59.8	58.5	29.3	26.3	25.2	18.8	15.8	14.4

TABLE III

Maximum Tensile and Compressive Stresses in the Fillet at the Root of the Tooth Affected by the Value of P_n mand ψ Value for $\phi_n = 14.5^\circ$

P_n	80			32			16		
ϕ_n	14.5°	22.5°	30°	14.5°	22.5°	30°	14.5°	22.5°	30°
σ_{tmax}	107.8	126.1	184.6	51.8	59.3	85.6	36.7	40.4	54.3
σ_{cmax}	64.5	75.9	113.1	29.3	33.9	50.5	18.8	21.2	30.3

(2) The larger the value of P_n, the higher the distribution of stress.

The larger the value of P_n, the smaller the values of h and h_k, the larger the values of ϕ_r, r_{ct}, r_{nf}, and the smaller the values of l_t and l_c. Thus it leads to higher stress distribution.

(3) The lower the value of ϕ_n, the higher the distribution of stress. Since the smaller the value of ϕ_n, the narrower the tooth width, it results in higher stress distribution.

(4) The larger the value of ψ, the higher the distribution of stress.

(i) Since the larger ψ makes the larger r_n, higher stress distribution results.

(ii) The larger ψ makes the larger r_{ct}, and results in larger r_{nf}, while the smaller l_f and l_c are achieved; therefore it leads to higher stress distribution.

(5) As ψ increases, the contact pair of teeth will increase; hence the transmitted torque will increase too.

(6) (i) As $P_n = 32$, the value of ϕ_n decreases from 30° to 22.5° and 14.5°, respectively, the stress distribution increases from 1.27 to 1.48 times and from 1.67 to 2.20 times, respectively.

(ii) As $P_n = 32$, the value of ψ increases from 5° to 25° and 45° respectively, the stress distribution also increases from 1.08 to 1.14 times and from 1.25 to 1.65 times respectively. It is obvious that the stress distribution is affected more greatly by the variation of ϕ_n then by that of ψ.

(7) (i) As $\psi = 5^\circ$, the value of P_n increases from 16 to 32 and 80 respectively, the stress distribution also increases from 1.41 to 1.59 times and from 2.94 to 3.50 times respectively.

(ii) As $\phi_n = 14.5^\circ$, the value of P_n increases from 16 to 32 and 80 respectively, the stress distribution also increases from 1.41 to 1.58 times and from 2.94 to 3.50 times respectively.

(8) (i) Setting $P_n = 32$, when $\phi_n = 14.5°$ then $\sigma_{tmax} = 1.70 \sim 1.77\ \sigma_{cmax}$
when $\phi_n = 22.5°$ then $\sigma_{tmax} = 1.44 \sim 1.50\ \sigma_{cmax}$
when $\phi_n = 30°$ then $\sigma_{tmax} = 1.20 \sim 1.23\ \sigma_{cmax}$

(ii) Setting $\psi = 5°$, when $\phi_n = 14.5°$ then $\sigma_{tmas} = 1.67 \sim 1.95\ \sigma_{cmax}$
when $\phi_n = 22.5$ then $\sigma_{tmax} = 1.41 \sim 1.66\ \sigma_{cmax}$
when $\phi_n = 30°$ then $\sigma_{tmax} = 1.17 \sim 1.35\ \sigma_{cmax}$.

Conclusions

(1) The distribution of stress σ_t and σ_c are similar to the form of the contact surface pressure q.

(2) The tensile stress in the fillet at the root of the tooth has a maximum value for the variation of ψ, ϕ_n, and P_n at about $x = -0.2a$, while the maximum compressive stress occurs at about $x = +0.2a$.

(3) The larger the value of P_n, the higher the distribution of stress.

(4) As ψ increases, both the distribution of stress σ_t and σ_c and the transmitted torque increases.

(5) As ϕ_n increases, there wil be higher distribution of stress σ_t and σ_c.

(6) The stress distribution is affected more greatly by the variation of ϕ_n than by that of ψ.

Appendix: Nomenclature

Z	active portion of line of action
Z_q	distance along the line of action to a general contact point
Z_r	recess portion of the line of action
a	semi-major axis of contact ellipse
b	semi-minor axis of contact ellipse
A	area of rectangular contact
E'	effective modulus of elasticity of gear pair
E_1	modulus of elasticity of pinion
E_2	modulus of elasticity of gear
F	face width
G	gear ratio
K	effective profile radius coefficient
K_1	profile radius coefficient of pinion
K_2	profile radius coefficient of gear
P	pitch point
P_n	normal diametral pitch
R_1	pitch radius of pinion

R_2 pitch radius of gear
R_e equivalent radius of curvature of generating pitch circle
R_{nr} gear tooth root radius in normal plane
R_{o1} outside radius of pinion
R_{o2} outside radius of gear
d_e distance from contact point to center of fillet radius on compression side of tooth
d_t distance from contact point to center of fillet radius on tension side of tooth
h adendum height
h_b dedendum height
h_k distance from hob pitch-line to tangent point of hob tip radius
l_c distance from wedge apex to tangent point on compression fillet
l_f radius from pinion center to center of tooth fillet radius
l_t distance from wedge apex to tangent point on tension fillet
λ_e angle between line u_{nq} and line d_c
λ_t angle between line u_{nq} and line d_t
ν_1 Poisson's ratio of pinion material
ν_2 Poisson's ratio of gear material
ξ_c angle between side of wedge and line from apex to compression-fillet center
ξ_t angle between side of wedge and line from apex to tension-fillet center
ρ_t transverse radius from pinion center to profile arc center
ρ_{n_1} normal radius from pinion center to profile arc center
σ_c compressive stress at tangent point of inscribed wedge and tooth fillet
σ_r radial stress in wedge
σ_t tensile stress at tangent point of inscribed wedge and tooth fillet
W total load per contact ellipse
n_1 number of teeth in pinion
n_2 number of teeth in gear
q Hertzian contact stress
q_o maximum Hertzian contact stress
r radial coordinate
r_1 transverse radius of pinion tooth profile
r_2 transverse radius of gear tooth profile
r_{ct} radius of hob tip
r_n relative radius of normal profile curvature
r_{n_1} normal radius of pinion tooth profile
r_{n_2} normal radius of gear tooth profile
r_{nf} normal radius of pinion tooth fillet
r_{nh} normal radius of hob profile
u_{nq} normal radius vector of point of contact
w inclination angle of helical contact line
w_x load per inch of contact
x abscissa along major axis of contact ellipse
x' abscissa along pitch helix
y ordinate along minor axis of contact ellipse
y' ordinate in the tangent plane and perpendicular to pitch helix
z ordinate perpendicular to tangent plane

α transverse angle between pitch plane and surface of action. Wedge half-angle.
α_1 transverse angle between line of centers and line from pinion center to profile arc center
α_2 transverse angle between line of centers and line from gear center to profile arc center
β angle between load vector and wedge center line
β_{nq} angle between normal pressure line and line ρ_{n1}
γ_1 half-angle between tooth center line and tooth space center line
γ_{n_1} angle γ_1 in normal plane
η included angle of wedge
η_c angle between load vector and compression side of wedge
η_t angle between load vector and tension side of wedge
ϕ transverse pressure angle
ϕ_n normal pressure angle
ϕ_q normal pressure angle at point of contact
ϕ_r normal pressure angle at tangent point of the hob tip radius and hob profile radius
ψ helix angle in the pitch plane
ψ' helix angle in the surface of action

References

1. W. Lewis, "Investigation of the Strength of Gear Teeth," Proceeding of the Engineers Club, Philadelphia, PA, 1893.
2. German Standard DIN 3990, "Load Capacity Computation of Spur and Bevel Gears," 1970.
3. T. J. Dolan and E. L. Broghamer, "A Photoelastic Study of the Stresses in Gear Tooth Fillets," University of Illinois, Engineering, Experiment Station Bulletin No. 335, 1942.
4. E. J. Wellauer and A. Seireg, Bending stress of gear teeth by cantilever plate theory, *J. Engrg. Ind. Trans ASME* (1960).
5. AGMA Std 221.02, "Rating the Strength of Helical and Herringbone Gear Teeth," 1965.
6. AGMA Std 220.02 "Strength of Spur Gear Teeth," 1966.
7. Nieman, "Machine Elements," Vol. II, Springer, Berlin, 1960.
8. Nieman and Glaubitz, "Dedendum Strength of Steel Spur Gears," p. 923, VDI-Zeitschrift, 150.
9. Heywood, "Tensile Fillet stresses in Loaded Projections," Proceedings, Inst. Mech. Eng. 159, 1948.
10. G. Chabert, T. D. Tran, and R. Mathis An evaluation of stresses and deflection of spur gear teeth under strain, *J. Engrg. Ind. Trans. ASME* (1974).
11. S. K. Chan and I. S. Tuba, A finite element method for contact problems of solid bodies, *Internat. J. Mech. Sci.* **13** (1971), 615–625.
12. G. Castellani and V. P. Castelli, Rating gear strength, *J. Mech. Design Trans. ASME* (1981).
13. H. Winter and M. Hirt, The measurement of actual strains at gear teeth, influence of fillet radius on stresses and tooth strength, *J. Engrg. Ind. Trans. ASME* (1974).
14. B. A. Shotter, "A New Approach to Gear Tooth Root Stresses," ASME Paper No. 72-PTG-42, 1972.
15. Aida and Terauchi, "Bending Fatigue Breakage of Gear Teeth," Trans. Semi-International Symp., No. 1, p. 217, 1967.

16. ALBERT AND OBENAUS, "Influence of Tooth Parameters on Tooth Strength," Antriebstechnik 6, No. 10, p. 384, 1967.
17. R. ERRICHELLO, Bending stress in gear teeth having circular arc profile—Part 1 analysis, *J. Mech. Design Trans. SME* (1978).
18. D. W. DUDLEY, "Practical Gear Design," McGraw-Hill, New York, 1954.
19. S. TIMOSHENKO AND J. N. GOODIER, "Theory of Elasticity," 2nd. ed., McGraw-Hill, New York, 1951.
20. F. B. SEELY AND J. O. SMITH, "Advanced Mechanics of Materials," 2nd ed., pp. 342–378, Wiley, New York, 152.